nature physics

Article

https://doi.org/10.1038/s41567-025-03131-0

Strong correlations and superconductivity in the supermoiré lattice

Received: 19 December 2024

Accepted: 7 November 2025

Published online: 20 January 2026

Check for updates

Zekang Zhou[1], Cheng Shen[1], Kryštof Kolář[2], Kenji Watanabe[3], Takashi Taniguchi[4], Cyprian Lewandowski[5,6] & Mitali Banerjee[1,7]

The supermoiré lattice, arising from the interference of multiple moiré patterns, reshapes the electronic band structure of the material that hosts it by introducing new mini bands and modifying the band dispersion. Concurrently, strong electronic interactions within the flat bands induced by the moiré pattern lead to the emergence of various correlated states. However, the impact of the supermoiré lattice on the flat band system with strong interactions remains largely unexplored. Here we report the existence of the supermoiré lattice in twisted trilayer graphene with broken mirror symmetry and elucidate its role in generating mini flat bands and mini Dirac bands. We demonstrate interaction-induced symmetry-broken phases in the supermoiré mini flat bands alongside a cascade of superconductor–insulator transitions enabled by the supermoiré lattice. Our work shows that robust superconductivity can exist in twisted trilayer graphene with broken mirror symmetry and underscores the importance of the supermoiré lattice as an additional degree of freedom for tuning the electronic properties in twisted multilayer systems. It also sheds light on the correlated quantum phases such as superconductivity in the original moiré flat bands, and highlights the potential of using the supermoiré lattice to design and simulate quantum phases.

The family of two-dimensional moiré materials has recently emerged as a near-perfect platform for discovering and systematically exploring a wide range of quantum states of matter. Beginning with the observation of fractal physics of Hofstadter's butterfly[1–4], the study of moiré systems now has extended to the realization and simulation of intriguing correlated quantum states involving superconductivity and topological (fractional) quantum anomalous/spin Hall effect and so on[5–11]. The tunability of two-dimensional systems allowed us to consistently push the frontiers of studying moiré physics by introducing new experimental methods of control. Here we focus on one such technique: the realization of a supermoiré pattern.

The general form of the alternating-angle twisted trilayer graphene (TTG) can be obtained by stacking and twisting three layers of graphene, where the relative angles $\theta_{1,2}$ and $\theta_{2,3}$ between layers 1 and 2 and layers 2 and 3 satisfy $\theta_{1,2}\theta_{2,3} < 0$ (refs. 12,13). A special and most frequently studied configuration of TTG is the symmetric configuration $\theta_{12} = -\theta_{23}$, where the single-particle electronic spectrum has exactly one twisted bilayer graphene (TBG)-like flat band that is decoupled from a dispersive Dirac cone[12,14]. When $\theta_{12} = -\theta_{23} \approx \sqrt{2}\theta_{\mathrm{magic}}$ (here θ_{magic} is the magic angle of TBG)[12,14], the system exhibits overall similar experimental phenomenology to the TBG, featuring interaction-driven insulating phases and superconductivity[15–20]. Away from the symmetric twist-angle condition, when the two moiré lattices formed by adjacent layers are nearly commensurate, satisfying $p\theta_{12} \approx q\theta_{23}$, where p and q are integers, their interference results in an approximate supermoiré lattice with an effective moiré wavevector given by $|\mathbf{g}_{\mathrm{sm}}| \approx |\mathbf{g}_{12}|/q \approx |\mathbf{g}_{23}|/p$

[1]Institute of Physics, Ecole Polytechnique Fédérale de Lausanne, Lausanne, Switzerland. [2]Dahlem Center for Complex Quantum Systems and Fachbereich Physik, Freie Universität Berlin, Berlin, Germany. [3]Research Center for Functional Materials, National Institute for Materials Science, Tsukuba, Japan. [4]International Center for Materials Nanoarchitectonics, National Institute for Materials Science, Tsukuba, Japan. [5]National High Magnetic Field Laboratory, Tallahassee, FL, USA. [6]Department of Physics, Florida State University, Tallahassee, FL, USA. [7]Center for Quantum Science and Engineering, Ecole Polytechnique Fédérale de Lausanne, Lausanne, Switzerland. e-mail: mitali.banerjee@epfl.ch

($\mathbf{g}_{12}$ and $\mathbf{g}_{23}$ are the moiré wavevectors of two moiré lattices). For p and q consecutive integers, the new supermoiré length scale can be written as $\lambda_{sm} = a/\theta_{13}$, where a is the lattice constant and θ_{13} is the twist angle between the outer layers. The presence of the supermoiré lattice has been observed in twisted trilayer systems through techniques such as conductive atomic force microscopy, scanning tunnelling microscopy, scanning transmission electron microscopy and thermodynamic measurements[21–28]. However, experimental transport measurements on supermoiré lattices are still limited.

This work explores the intricate interplay between the supermoiré lattice, original moiré flat bands with strong electronic interactions and dispersive Dirac bands. We confirm the presence of the supermoiré lattice through electronic transport measurements by observing the Brown–Zak oscillation and Hofstadter's butterfly stemming from the formation of the supermoiré lattice. Moreover, we observe isospin-symmetry-broken phases within the supermoiré mini flat bands and robust superconductivity that is strongly modulated by the supermoiré potential. Our work highlights the importance of the supermoiré lattice in reshaping the electronic band structure and correlated physics of twisted multilayer systems and offers fresh insights into the emergent physics of moiré materials.

Mirror-symmetry-broken TTG

Figure 1a illustrates the double-gate geometry of the device, where the carrier density (n) and displacement field (D) can be tuned independently (Methods provides the device fabrication process). In a typical TTG device in which $\theta_{12} = -\theta_{23}$, mirror symmetry is expected[12,14], leading to a symmetric n–D phase diagram with respect to the $D = 0$ V nm^{-1} line[15–20] (Extended Data Fig. 1a,b shows the ν–D mapping, where υ is the moiré filling factor, for a mirror-symmetric TTG device with a twist angle of 1.35°). However, our measurements (Fig. 1b) show asymmetrical results of longitudinal resistance R_{xx} between D and $-D$, indicating the absence of mirror symmetry. Taken together with the absence of TTG and hexagonal boron nitride (hBN) alignment (Supplementary Section 2), this suggests that $\theta_{12} \neq -\theta_{23}$ and the mirror symmetry is broken in the device. This conclusion is further supported by the n–D map (Fig. 1b), which shows a large number of resistive peaks and zero-resistance domes spanning across a broad charge density region on both electron and hole sides. This is in stark contrast to the mirror-symmetric TTG, where the onset of correlated states is well defined by integer moiré fillings (Extended Data Fig. 1).

To thoroughly characterize the resistive states and confirm the twist angles present in the device, we conduct magnetic field dependence measurements. Figure 1d,e presents the Landau fan diagrams of R_{xx} and the Hall resistance R_{xy} at $D = 0$ V nm^{-1}, with a summary shown in Fig. 1f. We categorize the observed Landau fans into three sets: states due to the bottom moiré lattice, states hosted by the top moiré lattice and states arising from the supermoiré lattice. From the full-filling carrier density of the single moiré lattice, twist angles can be extracted by using the expression $n_f = 8\theta^2/\sqrt{3}a^2$, yielding $\theta_{12} = 1.328°$ and $\theta_{23} = -1.785°$ (here n_f is the full-filling carrier density of the single moiré lattice; Supplementary Section 3 provides more details on how to define the full-filling carrier density of two moiré lattices). The extracted unequal twist angles confirm the lack of mirror symmetry and the presence of two moiré patterns within the system (Fig. 1b). In particular, several Landau fans are incommensurate with the full-filling set by the top or bottom moiré lattice (Fig. 1f, purple lines). We interpret them as Landau-level states stemming from the emergent supermoiré mini bands (Fig. 1c).

Before proceeding with further analysis, we want to pause and place our work in the larger context of previously reported results in the literature on the alternating-angle TTG away from the symmetric twist-angle condition. In ref. 29, the two twist angles are 1.4° and −1.9° with the superconductivity (and other electronic transport measurements) interpreted as emerging from the moiré quasicrystal formation rather than the formation of a supermoiré lattice. In ref. 27, on the other hand, the presence of a supermoiré lattice with a twist-angle difference of 0.43° is reported. The system is studied using compressibility measurements and presents multiple incompressible states attributed to the presence of the supermoiré lattice. Our measurements, thus, complement these existing experiments reporting on the transport manifestation of the isospin symmetry breaking and the observation of superconductivity in the supermoiré regime.

Supermoiré-lattice-induced Hofstadter's butterfly and supermoiré mini bands

The interference between two moiré lattices can give rise to a well-defined supermoiré lattice. Indeed, the presence of the supermoiré lattice in our system can be confirmed with the low-field Brown–Zak oscillations[30–32], which exhibit conductance oscillations arising from the interplay between the magnetic flux and the supermoiré potential. Figure 2a is the zoomed-in view of the Landau fan diagram of R_{xx} near full-filling density n_{12}. R_{xx} dips (conductance peaks) at a constant magnetic field are observed at an applied magnetic field $B = 2.5$ T, 1.7 T, 1.25 T and 1 T (red dashed lines), which corresponds to 1/2, 1/3, 1/4 and 1/5 quantum flux of the unit cell with a spatial period $\lambda_{sm\text{-}exp} = 30.6$ nm (Extended Data Figs. 2 and 3). This length scale is in agreement with the expected supermoiré length of $\lambda_{sm\text{-}cal} = a/\theta_{13} = a/(\theta_{12} + \theta_{23}) = 30.8$ nm. As shown in Supplementary Section 2, we have ruled out the existence of a moiré lattice between hBN and graphene. In addition to observing the Brown–Zak oscillation, the Landau-level states stemming from 5 T towards the high- and low-magnetic-field sides (Fig. 2a, black dashed lines) confirm the identification of $B = 5$ T as corresponding to one quantum flux within the supermoiré unit cell.

Similar to the physical picture of band folding by the original moiré lattice, the supermoiré lattice will further fold and tailor the moiré bands into mini bands (Fig. 1c). As a result of the secondary band folding, we expect the appearance of additional Landau fans. To search for this effect, we look more closely at Fig. 2b–d of the Hall resistance R_{xy} in the region between the full-filling densities of $-n_{23}$ and $-n_{12}$ on the hole side (Fig. 2b), near the charge neutrality point (CNP; Fig. 2c) and in the region between n_{12} and n_{23} on the electron side (Fig. 2d).

In Fig. 2b (marked by dashed lines), three sets of Landau fans are visible. The charge density spacing between these sets of Landau levels is $0.95n_{sm}$ and n_{sm} (where $n_{sm} = 4/(\sqrt{3}/2 \times \lambda_{sm}^2) = 4.83 \times 10^{11}$ cm^{-2} is the full-filling carrier density of supermoiré mini bands). In Fig. 2c, in addition to the Landau fan originating from the CNP, another state marked (marked by the red dashed line) appears in a finite magnetic field, and the charge density spacing between this state and the CNP also corresponds to n_{sm}. In Fig. 2d, four sets of Landau fans exist in this region, and the charge density spacing between each is n_{sm}. Furthermore, as shown in Extended Data Fig. 4, R_{xx} shows repeated oscillations with the charge density equal to n_{sm}. All these observations indicate that the supermoiré potential indeed further folds the original moiré bands into mini bands. We note that the carrier density between supermoiré-lattice-induced states can exhibit small variations from case to case. Although the precise origin of this small variation is not fully clear, we include error bars in n_{sm} and define full filling as $n_{sm}(1 \pm 5\%)$. Hereafter, n_{sm} includes this small uncertainty.

In addition to the supermoiré potential's role on the original moiré flat bands, it is interesting to explore the fate of the Dirac cone in this trilayer system. As explained earlier, at the symmetric-angle condition, TTG is expected to host a Dirac cone that is decoupled from the flat bands. We can, thus, use a Dirac cone in our system as a perturbation to the Dirac cone of the symmetric TTG. Alternatively, we can think of the Dirac cone in our system as the original Dirac cone of the third layer when brought in proximity to the moiré system of layers one and two. In either case, the supermoiré potential is expected to fold the Dirac band, producing satellite Dirac points resembling the graphene/hBN moiré superlattice[1–3].

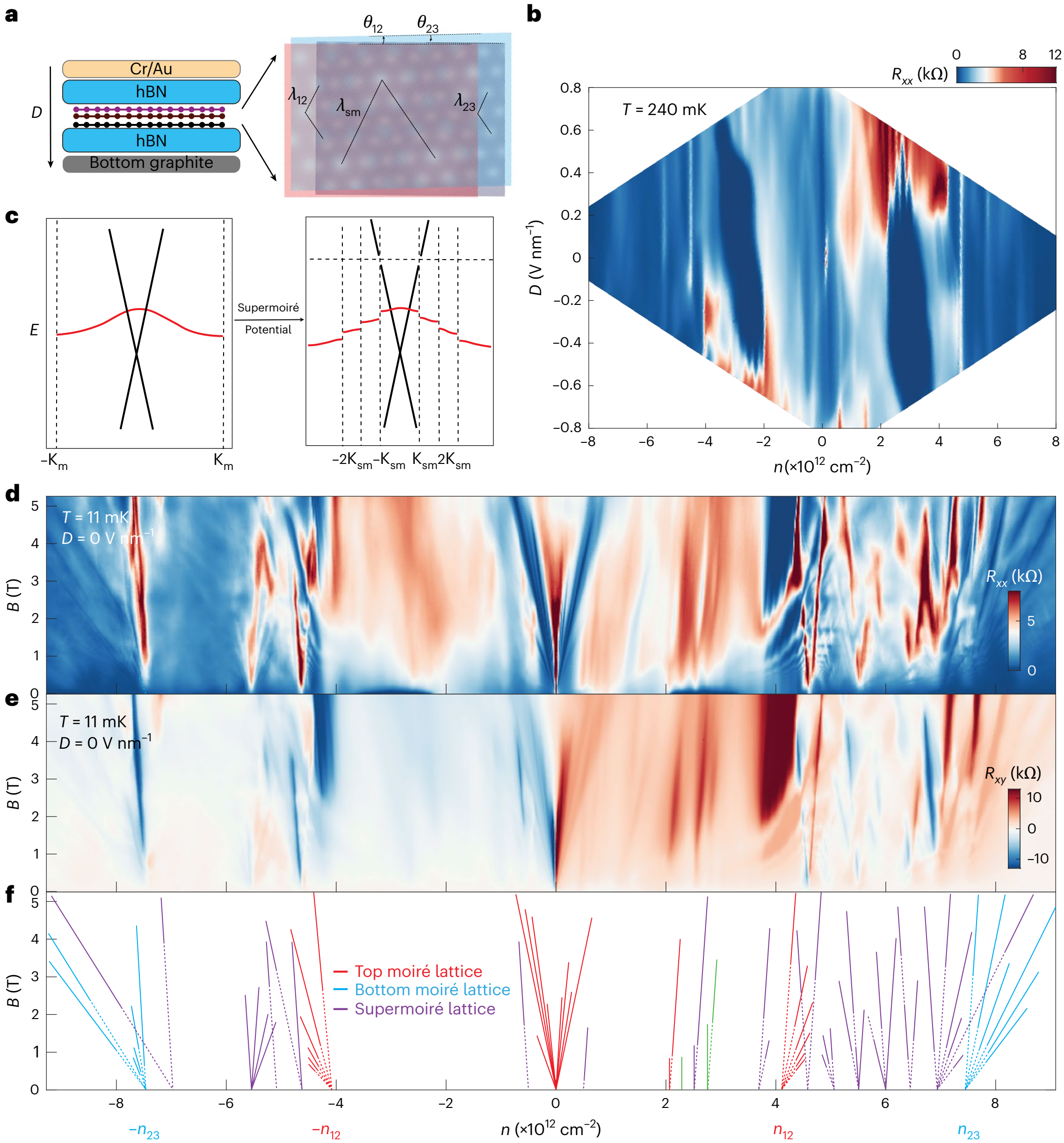

Fig. 1 | Mirror-symmetry-broken TTG. a, Schematic of the device with double gates to tune the carrier density and displacement field independently. Right: moiré pattern of the mirror-symmetry-broken TTG, consisting of two small moiré lengths λ_{12} and λ_{23} and a large supermoiré length λ_{sm}. **b**, Longitudinal resistance R_{xx} as a function of n and D measured at T = 240 mK. R_{xx} shows zero resistance and many resistive states in a large region in the n–D mapping. **c**, Schematic illustrating the impact of the supermoiré lattice on the band structure. Left: sketch of the band structure of TTG; the flat bands coexist with a dispersive Dirac band, and the Fermi velocity of the Dirac band is far larger than that of the flat band. Right: band structure after band folding by the supermoiré lattice. The original moiré flat band is diced into mini flat bands in the supermoiré Brillouin zone. Also, the Dirac band is folded to form the satellite Dirac points. E, energy; K_m, boundary of the moiré Brillouin zone; K_{sm}, boundary of the supermoiré Brillouin zone. **d**,**e**, Landau fan diagram of R_{xx} and R_{xy} at D = 0 V nm^{-1} at T = 11 mK. **f**, States shown in **d** and **e**. The blue lines denote the Landau fan emanating from the full filling of the bottom moiré lattice $\pm n_{23}$; the red lines denote the Landau fan stemming from the CNP, half-filling correlated state and band insulators of the top moiré pattern; the purple lines represent the Landau levels from the supermoiré-lattice-induced states; and the green lines mark the half-filling correlated states of the supermoiré mini bands.

The satellite Dirac points have much higher energy than the flat bands at D = 0 V nm^{-1} since the Fermi velocity of the Dirac band is close to 10^6 m s^{-1} (ref. 33; Fig. 1c and Extended Data Fig. 5). By tuning the displacement field, we can change the energy of the satellite Dirac points compared with the Fermi level, allowing us to identify the satellite Dirac points. Figure 2e,f shows R_{xx} and R_{xy} as a function of n and D at B = 5 T near the CNP, respectively. The results show vertical zero R_{xx} features intersected by multiple S-shaped curves, which implies multiband electronic transport behaviour in the system. We attribute the vertical features to the Landau-level states originating from flat bands. Charge density spacing between each vertical line equals $4eB/h$, which suggests four-fold degeneracy due to the spin and valley degrees of freedom in the flat bands (the degeneracy can be lifted by increasing the magnetic field; Extended Data Fig. 6). The S-shaped features, however, are the Dirac Landau-level transition lines, between which $N_{Dirac} = \pm10, \pm6$ and ±2 Dirac Landau levels are filled. At a constant total carrier density, varying the displacement field results in an adjustment of the electron density within the Dirac band, transitioning from $2eB/h$ to $6eB/h$ and $10eB/h$..., where h is Planck's constant and e is the electron charge, whereas the carrier density within the flat bands undergoes corresponding

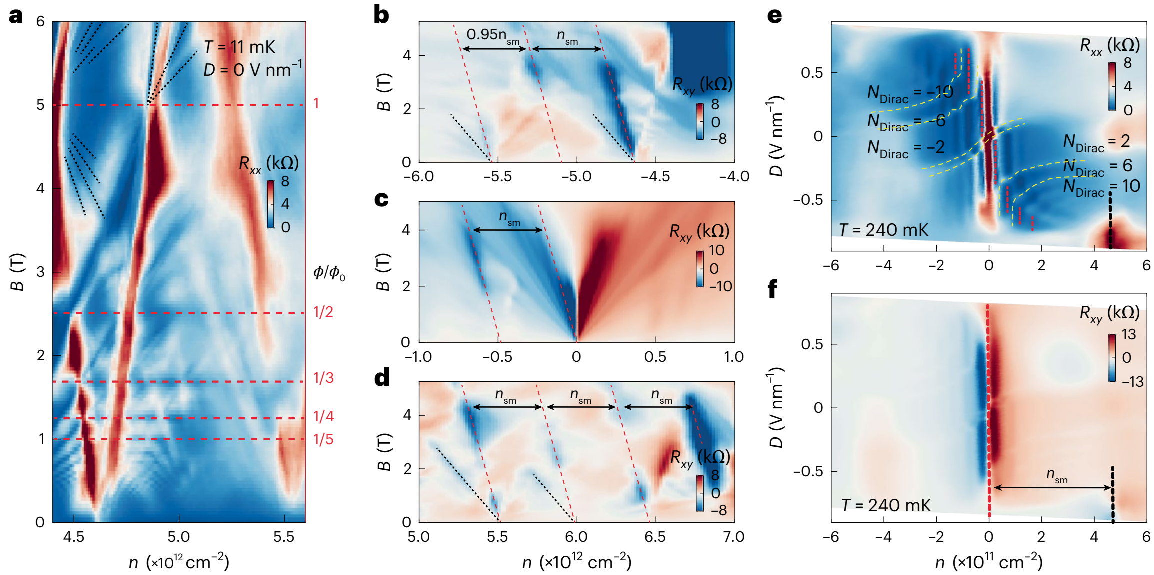

Fig. 2 | Supermoiré-lattice-induced Brown–Zak oscillation, Hofstadter's butterfly, and mini flat bands and mini Dirac bands. **a**, Landau fan diagram of R_{xx} at $D = 0$ V nm^{-1} shows Hofstadter's butterfly and Brown–Zak oscillations induced by the supermoiré lattice. The red dashed lines mark 1, 1/2, 1/3, 1/4, 1/5 quantum flux of the supermoiré lattice. The black dashed line shows the Landau levels originating from one quantum flux. ϕ, magnetic flux per supermoire lattice unit cell; ϕ_0, flux quantum. **b**–**d**, Zoomed-in view of the Landau fan diagram on the hole side between $-n_{23}$ and $-n_{12}$ (**b**), near the CNP (**c**) and on the electron side between n_{12} and n_{23} (**d**). The red dashed lines mark the pronounced states, and the distance between the states is n_{sm}; this signifies the existence of supermoiré mini bands. The black dashed lines correspond to Landau levels with Chern number −6. **e**,**f**, R_{xx} (**e**) and R_{xy} (**f**) as a function of n and D close to the CNP when $B = 0.5$ T. The red dashed line tracks the CNP of flat bands, and the black dashed line marks the state emerging from Dirac band folding.

adjustments. This process occurs as the displacement field adjusts the relative energy between the Landau-level states of the flat bands and those of the Dirac band. When the Hall resistance R_{xy} is quantized at $R_{xy} = h/(N_{Dirac}e^2)$ in the region where N_{Dirac} Dirac Landau levels are filled, the contribution of Hall density from the flat bands is zero. This fact, in turn, indicates that the Fermi level is at the CNP or in the correlated gaps of the flat bands, allowing us to track the CNP of the flat bands in the n–D map (Fig. 2e, red dashed line). Along the trace of the CNP of flat bands, one R_{xx} peak emerges with a sign change in the corresponding R_{xy} when the carrier density is equal to n_{sm} at $D = -0.6$ V nm^{-1} (Fig. 2e,f, black dashed lines), indicating a satellite Dirac point.

Interaction-induced isospin-symmetry-broken phases in supermoiré mini flat bands

Having confirmed the presence of secondary supermoiré band folding, we now discuss the role of interaction effects in these mini bands. The original moiré flat bands exhibit correlated electronic phases due to the dominant Coulomb interactions over kinetic energy. Supermoiré bands further quench the kinetic energy, but since the same supermoiré length-scale factor lowers the characteristic Coulomb energy scale, the ratio between Coulomb interactions and the bandwidth of the supermoiré mini flat bands remains similar to that of the original moiré flat bands. Therefore, mini flat bands can also host correlated phases. To demonstrate the presence of symmetry-broken states, we will now consider R_{xx} versus n and B near full filling of the top moiré lattice n_{12} on the electron side (Fig. 3a).

The phase diagram shown in Fig. 3a can be understood by considering the role of interactions in shaping the interplay between the supermoiré lattice, moiré flat bands and Dirac bands. Figure 3b illustrates all the states appearing in Fig. 3a, and Fig. 3c shows the idealized sketch of the band structure in this region for clarity of discussion. The result shown in Fig. 3a can be divided into four regions based on the position of Fermi level, which we mark in Fig. 3b,c as (i)–(iv).

In region (iii) at point N, the Fermi level lies at the top of the top moiré flat bands. However, the electron density at point N does not equal to the full-filling carrier density of the top moiré lattice n_{12} because some electrons reside in the Dirac band. As the electron density increases, the Fermi level enters the moiré bandgap of the flat bands, and all electrons originate from the Dirac band. This regime is characterized by well-defined Dirac Landau levels with a sequence $N_{Dirac} = 2, 6, 10$... (Fig. 3b, black lines). Extending these Dirac Landau levels to zero magnetic fields defines point E, which gives the full-filling electron density of the top moiré lattice $n_{12} = n_E$. When the electron density continuously increases, the Fermi level will eventually lie at the satellite Dirac point (point P). A resistive R_{xx} peak appears at point P, and the Landau levels also emanate from point P. The Dirac band electron density at point P is $n = n_P - n_E$, which exactly equals n_{sm}, confirming the nature of point P as the satellite Dirac point.

In region (ii), both Dirac band and flat bands are partially occupied, with the majority of electrons residing in the flat bands owing to their enhanced density of states. Transitions between different Dirac Landau levels are visible (Fig. 3b, dashed pink lines; Extended Data Fig. 7a,b shows the corresponding R_{xy}). At point M, a gap opens in the moiré flat bands due to the supermoiré potential, and an isolated supermoiré mini flat band with four-fold degeneracy is formed. The supermoiré gapped state at point M exhibits a slope of N_{Dirac} in the fan diagram (Fig. 3b, red lines). Extending the Landau levels to zero magnetic field defines point A corresponding to the actual electron density n_A filled into flat bands at point M (we point out that we ignore the small contribution from the increase in the Dirac band carrier density when the Fermi level moves across the gap). The electron density difference in moiré flat bands between point M (where the Fermi level lies in the supermoiré gap) and point N (where the Fermi level lies at the top of the flat bands) is $n_E - n_A$, which is also equal to n_{sm}; this suggests that the states marked by the red lines are indeed the single-particle bandgap state of the supermoiré mini band.

In the R_{xx} diagram shown in Fig. 3a,b, three groups of Landau fans (highlighted by yellow, green and cyan lines) are observed, which cannot be explained by single-particle physics. We find that these Landau fans' zero-field charge density intercepts are equally spaced, with the charge spacing corresponding to a quarter full filling ($(1/4)n_{sm}$) of the supermoiré mini flat band. We interpret these states as

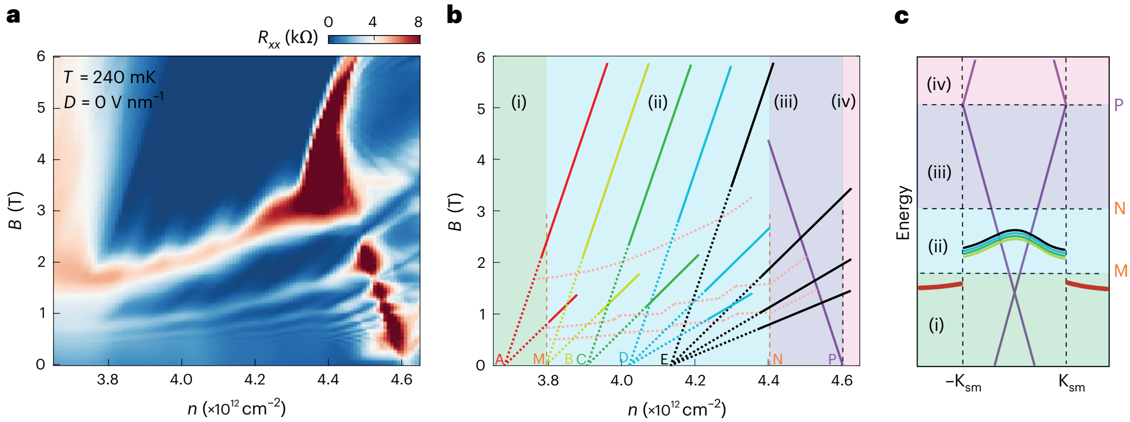

Fig. 3 | Interaction-induced isospin-symmetry-broken phases in mini flat bands. a, Landau fan diagram of R_{xx} at $D = 0$ V nm^{-1} near full filling n_{12} of the top moiré lattice. **b**, Guiding lines of the gapped states appearing in the R_{xx} map in **a**. The black lines mark the Landau fan from full filling of the top moiré lattice. Furthermore, four sets of Landau fans are marked by red, yellow, green and cyan lines, each with slopes of 2 and 6. The purple line shows the Landau levels from the satellite Dirac cone. The phase diagram can be categorized into four regimes based on the Fermi level position: (i) the Fermi level is below the single-particle gap opened in the moiré flat band by the supermoiré lattice potential; (ii) the Fermi level lies within the supermoiré mini-flat band; (iii) the Fermi level is located within the moiré gap of the flat band, where the Dirac band contributes to the transport behaviour; (iv) the Fermi level lies above the band folding point of the Dirac band. **c**, Sketch of the band structure in **a** and **b**.

isospin-symmetry-broken states arising from interactions within the supermoiré mini band. In analogy to the earlier analysis[18,34], the slope of the Landau levels from these mini band states at quarter filling is sensitive to the filling of the Landau levels from the Dirac band. These results highlight the crucial role played by the supermoiré potential in promoting symmetry breaking. As expected, in the absence of a supermoiré and additional band folding near the full filling of moiré flat bands, isospin symmetry breaking does not occur. However, when the bands are further modified by the presence of an additional translational symmetry breaking (here the supermoiré lattice), it can enable isospin-symmetry-broken phases. Extended Data Fig. 8 shows the isospin-symmetry-broken phases in the supermoiré mini band at a different displacement field.

We briefly comment on the apparent robustness of the decoupled Dirac band to hybridization with the mini bands. Carrying out a standard continuum model analysis[35–39] to obtain local band structures (Extended Data Fig. 5) suggests that away from the symmetric twist-angle condition, a strong hybridization between the mini bands and the Dirac cone should exist. As such, one would not expect a well-defined Dirac cone. The presence of a Dirac cone is in agreement with the prior work of ref. 29, for which it has been proposed to arise due to the Coulomb interaction[40]. Here we propose that this robustness of the Dirac cone could be explained by an unequal tunnelling strength between layers 1 and 2 and layers 2 and 3 (Extended Data Fig. 5). This reasoning is in line with recent theoretical works[13] that suggest that an alternating TTG tends to relax to symmetric TTG conditions, thereby accounting for the robustness of the Dirac cone.

Cascade of superconductor–insulator transitions

We now proceed to the impact of the supermoiré lattice on superconductivity. Robust superconductivity has been observed in multiple alternating TTGs in the symmetric twist-angle setup[15,16]; however, the observation of superconductivity in TTG away from this twist-angle regime remains rare. Previously, it was observed in a moiré quasicrystal TTG device[29], and we also report it here in the supermoiré TTG device. The mirror-symmetry-broken TTG exhibits superconductivity on both electron and hole sides (Fig. 4a). Figure 4b shows direct current voltage $V_{\mathrm{d.c.}}$ versus and direct current $I_{\mathrm{d.c.}}$ as a function of temperature (Fig. 4a, red star). The bottom-right inset shows the $V_{\mathrm{d.c.}}$–$I_{\mathrm{d.c.}}$ curve on a log–log scale, revealing that $V_{\mathrm{d.c.}}$ transitions from a high-power polynomial dependence to a linear dependence on $I_{\mathrm{d.c.}}$ as the temperature increases. The red dashed line shows $V_{\mathrm{d.c.}} \propto I^3_{\mathrm{d.c.}}$, signifying a two-dimensional superconducting Berezinskii–Kosterlitz–Thouless (BKT) transition at temperature $T = T_{\mathrm{BKT}} = 0.5$ K. The top-left inset shows R_{xx} as a function of temperature (the red dashed line is the T_{BKT} value extracted above), also demonstrating a typical superconductor behaviour.

Extended Data Fig. 9 provides further characterization of superconductivity. Figure 4a shows that resistive states extend into the superconducting dome at high displacement fields. We can characterize these resistive states as follows: half-filled correlated states of the top moiré bands ($(1/2)n_{12}$) shown by the red dashed lines or interaction-induced insulators stemming from half-filled or full-filled supermoiré mini bands ($(1/2)n_{12} + (1/2)Nn_{\mathrm{sm}}$, N is a positive number) shown by the green dashed lines. In contrast to the carrier density interval between resistive states in the high-doping region (Extended Data Fig. 4), the carrier density interval between these resistive states corresponds to half of the full filling ($n_{\mathrm{sm}}/2$) of supermoiré mini bands. Superconductivity is strongly modulated by these states, as shown by the bias current dependence measurement (Fig. 4c) and temperature dependence measurement (Fig. 4d), both measured at $D = 0.338$ V nm^{-1}. Extended Data Fig. 10 shows how this modulation of superconductivity evolves as a function of the displacement field.

The presence of intertwining insulators and superconductivity in the region $(1/2)n_{12} + (1/2)Nn_{\mathrm{sm}}$ is a particularly intriguing aspect of our work. We attribute this interplay between these two correlated phenomena to the complex competition between the effective supermoiré potential and interactions in the original moiré flat bands. This competition is illustrated in Fig. 4e, which highlights two distinct situations depending on the relative strengths of the supermoiré-induced gap and the interaction-induced gap.

- If the interaction-induced gap is much stronger than the supermoiré gap, then at $(1/2)n_{12}$, the four-fold degeneracy of the moiré flat bands is lifted first. Supermoiré mini flat bands, formed by Brillouin-zone folding of the two-fold degenerate moiré band, then host the same two-fold isospin degeneracy. In this case, the emergent insulators at $(1/2)n_{12} + (1/2)Nn_{\mathrm{sm}}$ are effectively single-particle insulators of the supermoiré flat bands. Each superconducting dome spans an entire mini flat band and has the same isospin order as others.

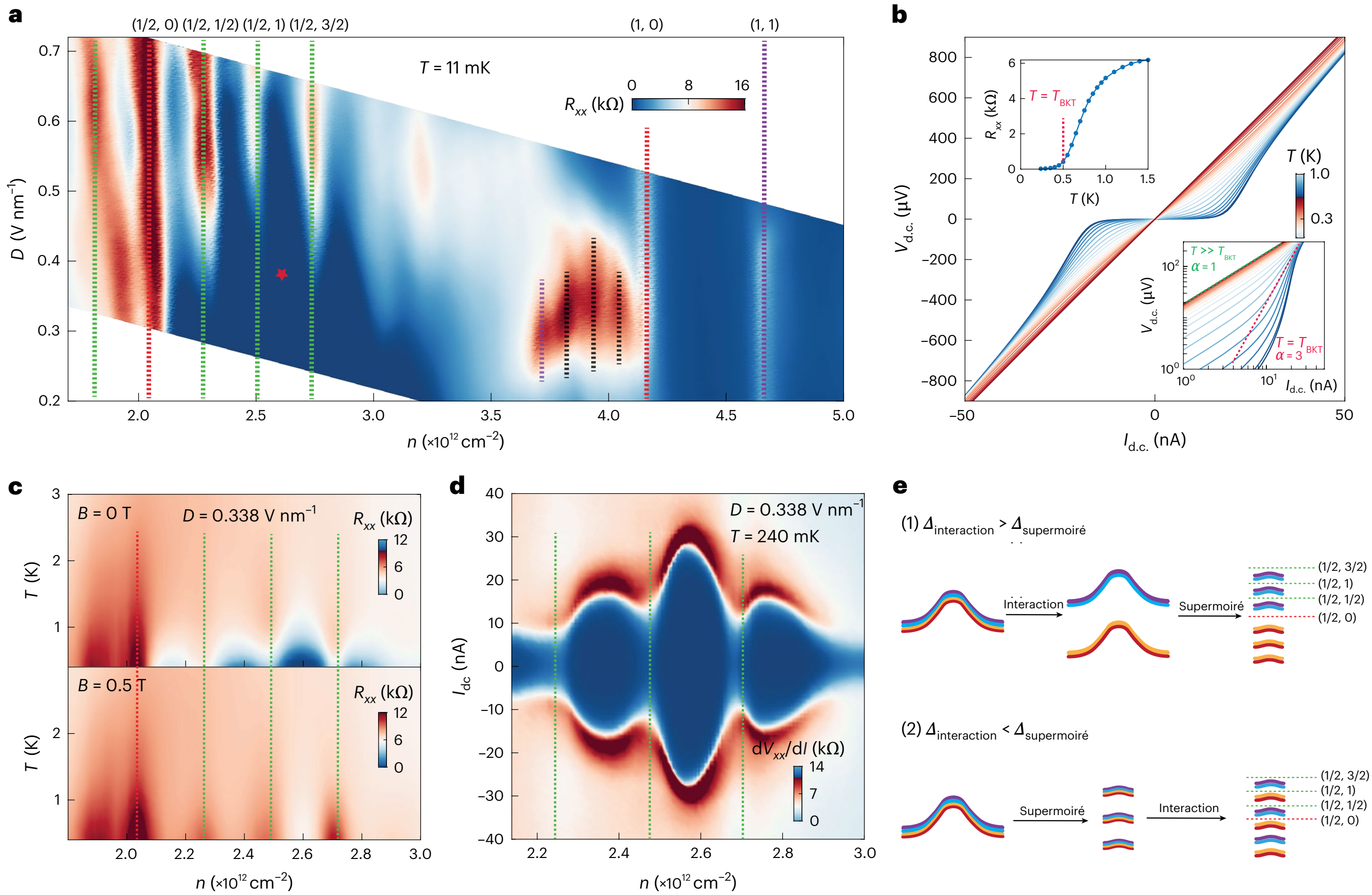

Fig. 4 | Cascade of superconductor–insulator transitions induced by the supermoiré lattice. a, Zoomed-in view of R_{xx} from Fig. 1b. The red dashed lines mark the half-filling and full-filling states of the top moiré flat bands; the green dashed lines mark the half-filling or full-filling states of the supermoiré mini bands. We also marked these states by using two numbers (x, y) when the states appear at the carrier density $n = (1/2)xn_{12} + (1/2)yn_{sm}$. **b**, $V_{d.c.}$–$I_{d.c.}$ curve as a function of temperature of the red star in **a**. Right-bottom inset: $V_{d.c.}$–$I_{d.c.}$ on a log–log scale; $V_{d.c.}$ follows a high-power polynomial to a linear dependence on $I_{d.c.}$ as the temperature increases. The green line shows $V_{d.c.} \propto I_{d.c.}$ when $T \gg T_{BKT}$; the red line shows $V_{d.c} \propto I^3_{d.c}$, indicating a BKT transition at this temperature. Top-left inset: R_{xx} as a function of T and the red dashed line is the T_{BKT} value. $α$, exponent of the fitting **c**, R_{xx} versus n and T when $B = 0$ T (top) and $B = 0.5$ T (bottom) at $D = 0.338$ V nm^{-1}. The superconducting dome is divided into several small domes in high displacement fields. High-resistance states emerge between the superconducting regions. The distance between these insulating states corresponds to half of the full filling of the supermoiré lattice. **d**, dV_{xx}/dI as a function of $I_{d.c.}$ and n at $D = 0.338$ V nm^{-1}. Three individual superconducting domes are visible. **e**, Two scenarios for the half-filling supermoiré insulator, with each colour representing a different isospin flavour. In the first scenario, the interaction within the moiré band is stronger than the supermoiré effect. The strong interactions first break the four-fold degeneracy, after which the supermoiré potential divides the moiré band into supermoiré mini flat bands. In the second scenario, the supermoiré potential dominates over the interaction. The supermoiré potential first divides the moiré band into a set of supermoiré bands, each with four-fold degeneracy. Then, the strong interaction within the supermoiré mini bands lifts the four-fold degeneracy. $Δ_{supermoiré}$, gap of supermoiré potential induced single pariticle gap; $Δ_{interaction}$, gap of the correlated states at half filling of supermoiré lattice.

- If the interaction-induced gap is much smaller than the supermoiré gap, then the supermoiré potential folds the moiré flat bands first, with each mini flat band having four-fold isospin degeneracy. This degeneracy is consequently lifted by interactions. In this scenario, the mini bands exhibit a cascade effect, similar to that in magic-angle TBG, but only at half-filling. Specifically, within one supermoiré mini band, the first half-filling maintains four-fold degeneracy, whereas the second half-filling reduces to two-fold degeneracy, except approaching the full filling of the supermoiré band. This implies that superconductivity in this case does not necessarily require isospin symmetry breaking.

Our findings highlight the potential of a supermoiré lattice in shaping the band structure and properties of correlated states in moiré systems. The intriguing coexistence of superconductivity with multiple insulating phases suggests that the further exploration of the TTG away from the symmetric twist-angle condition is needed. We propose that a systematic characterization of the nature of correlated phases in the supermoiré platform could potentially limit possible pairing mechanisms in the moiré graphene platform. Moreover, the supermoiré lattice is not limited to TTG but is a universal feature in moiré heterostructures. This opens up a new realm of experimental possibilities, as future multilayer devices focusing on other quantum states (such as the fractional Chern insulating states) could leverage this new degree of experimental freedom to realize yet another set of unexpected electronic quantum phases.

Online content

Any methods, additional references, Nature Portfolio reporting summaries, source data, extended data, supplementary information, acknowledgements, peer review information; details of author contributions and competing interests; and statements of data and code availability are available at https://doi.org/10.1038/s41567-025-03131-0.

References

1. Dean, C. R. et al. Hofstadter's butterfly and the fractal quantum Hall effect in moiré superlattices. *Nature* **497**, 598–602 (2013).
2. Hunt, B. et al. Massive Dirac fermions and Hofstadter butterfly in a van der Waals heterostructure. *Science* **340**, 1427–1430 (2013).
3. Ponomarenko, L. A. et al. Cloning of Dirac fermions in graphene superlattices. *Nature* **497**, 594–597 (2013).
4. Yankowitz, M. et al. Emergence of superlattice Dirac points in graphene on hexagonal boron nitride. *Nat. Phys.* **8**, 382–386 (2012).
5. Cao, Y. et al. Correlated insulator behaviour at half-filling in magic-angle graphene superlattices. *Nature* **556**, 80–84 (2018).
6. Cao, Y. et al. Unconventional superconductivity in magic-angle graphene superlattices. *Nature* **556**, 43–50 (2018).
7. Yankowitz, M. et al. Tuning superconductivity in twisted bilayer graphene. *Science* **363**, 1059–1064 (2019).
8. Serlin, M. et al. Intrinsic quantized anomalous Hall effect in a moiré heterostructure. *Science* **367**, 900–903 (2020).
9. Li, T. et al. Quantum anomalous Hall effect from intertwined moiré bands. *Nature* **600**, 641–646 (2021).
10. Park, H. et al. Observation of fractionally quantized anomalous Hall effect. *Nature* **622**, 74–79 (2023).
11. Lu, Z. et al. Fractional quantum anomalous Hall effect in multilayer graphene. *Nature* **626**, 759–764 (2024).
12. Zhu, Z. et al. Twisted trilayer graphene: a precisely tunable platform for correlated electrons. *Phys. Rev. Lett.* **125**, 116404 (2020).
13. Nakatsuji, N., Kawakami, T. & Koshino, M. Multiscale lattice relaxation in general twisted trilayer graphenes. *Phys. Rev. X* **13**, 041007 (2023).
14. Khalaf, E. et al. Magic angle hierarchy in twisted graphene multilayers. *Phys. Rev. B* **100**, 085109 (2019).
15. Park, J. M. et al. Tunable strongly coupled superconductivity in magic-angle twisted trilayer graphene. *Nature* **590**, 249–255 (2021).
16. Hao, Z. et al. Electric field–tunable superconductivity in alternating-twist magic-angle trilayer graphene. *Science* **371**, 1133–1138 (2021).
17. Cao, Y. et al. Pauli-limit violation and re-entrant superconductivity in moiré graphene. *Nature* **595**, 526–531 (2021).
18. Shen, C. et al. Dirac spectroscopy of strongly correlated phases in twisted trilayer graphene. *Nat. Mater.* **22**, 316–321 (2023).
19. Liu, X. et al. Isospin order in superconducting magic-angle twisted trilayer graphene. *Nat. Phys.* **18**, 522–527 (2022).
20. Zhou, Z. et al. Gate-tunable double-dome superconductivity in twisted trilayer graphene. *Nature Phys.* **21**, 1–7 (2025).
21. Li, Y. et al. Symmetry breaking and anomalous conductivity in a double-moiré superlattice. *Nano Lett.* **22**, 6215–6222 (2022).
22. Turkel, S. et al. Orderly disorder in magic-angle twisted trilayer graphene. *Science* **376**, 193–199 (2022).
23. Craig, I. M. et al. Local atomic stacking and symmetry in twisted graphene trilayers. *Nat. Mater.* **23**, 323–330 (2024).
24. Van Winkle, M. et al. Engineering interfacial polarization switching in van der Waals multilayers. *Nat. Nanotechnol.* **19**, 816–822 (2024).
25. Park, D. et al. Unconventional domain tessellations in moiré-of-moiré lattices. *Nature* **641**, 896–903 (2025).
26. Hao, C.-Y. et al. Robust flat bands in twisted trilayer graphene moiré quasicrystals. *Nat. Commun.* **15**, 8437 (2024).
27. Xie, Y. et al. Strong interactions and isospin symmetry breaking in a supermoiré lattice. *Science* **389**, 736–740 (2025).
28. Hesp, N. C. H. et al. Cryogenic nano-imaging of second-order moiré superlattices. *Nat. Mater.* **23**, 1664–1670 (2024).
29. Uri, A. et al. Superconductivity and strong interactions in a tunable moiré quasicrystal. *Nature* **620**, 762–767 (2023).
30. Brown, E. Bloch electrons in a uniform magnetic field. *Phys. Rev.* **133**, A1038–A1044 (1964).
31. Zak, J. Magnetic translation group. *Phys. Rev.* **134**, A1602–A1606 (1964).
32. Kumar, R. K. et al. High-temperature quantum oscillations caused by recurring Bloch states in graphene superlattices. *Science* **357**, 181–184 (2017).
33. Kim, H. et al. Evidence for unconventional superconductivity in twisted trilayer graphene. *Nature* **606**, 494–500 (2022).
34. Jiang, J. et al. Direct probing of energy gaps and bandwidth in gate-tunable flat band graphene systems. *Nat. Commun.* **16**, 1308 (2025).
35. Guerci, D., Mao, Y. & Mora, C. Chern mosaic and ideal flat bands in equal-twist trilayer graphene. *Phys. Rev. Res.* **6**, L022025 (2024).
36. Devakul, T. et al. Magic-angle helical trilayer graphene. *Sci. Adv.* **9**, eadi6063 (2023).
37. Mao, Y., Guerci, D. & Mora, C. Supermoiré low-energy effective theory of twisted trilayer graphene. *Phys. Rev. B* **107**, 125423 (2023).
38. Popov, F. K. & Tarnopolsky, G. Magic angle butterfly in twisted trilayer graphene. *Phys. Rev. Res* **5**, 043079 (2023).
39. Foo, D. C. W. et al. Extended magic phase in twisted graphene multilayers. *Phys. Rev. Res.* **6**, 013165 (2024).
40. Yang, C. et al. Multi-moiré trilayer graphene: lattice relaxation, electronic structure, and magic angles. *Phys. Rev. B* **110**, 115434 (2024).

Methods

Sample fabrication and measurements

The stacks are made by using the dry-transfer technique. Graphene, graphite and hBN are exfoliated on SiO_2/Si chips, and the thickness and quality of the materials are checked under an optical microscope. The long monolayer graphene is cut into three pieces before being picked up to reduce strain during the stacking process. A custom-made poly(bisphenol A carbonate)/polydimethylsiloxane stamp is used to pick up all the flakes one by one. The stack is finally dropped down on the aligned marker chips at 200°. Then, 5-nm/20-nm Cr/Au is evaporated on top of the stack to serve as the top gate and mask of the etch process. Furthermore, 5-nm/60-nm Cr/Au is evaporated to connect graphene to form one-dimensional contacts.

Electronic transport measurements are performed in two fridges. One is an Oxford He-3 fridge with a base temperature of T = 240 mK, and the other is a Bluefors dilution refrigerator with a base temperature of T = 11 mK. Resistance measurements are conducted using a standard lock-in technique using a 1–10-nA a.c. current excitation at a frequency of 17 Hz. Two Yokogawa GS200 devices are used to apply the top- and bottom-gate voltages to tune the carrier density and displacement field. Voltage signals are taken before being amplified 100 times.

Extraction of two twist angles

The twist angle is linked to full moiré carrier density by the relationship $N_f = 8\theta^2/\sqrt{3}a^2$, where a = 0.246 nm is the lattice constant of graphene. To get the full-filling carrier density, the Hall resistance is measured as shown in Supplementary Fig. 4a. We used antisymmetric $R_{xy} = (R_{xy}(B) + R_{xy}(-B))/2$ to reduce the effect of R_{xx} on R_{xy}. Supplementary Fig. 4b shows R_{xy} as a function of B at different top-gate voltage V_{tg} values and the Hall density at these V_{tg} values can be extracted through the relation $R_{xy} = B/(en)$. The carrier density in the device is determined by $n = (C_{tg}V_{tg} + C_{bg}V_{bg})/e$ and the displacement field is $D = (C_{tg}V_{tg} - C_{bg}V_{bg})/2\varepsilon_0$, where V_{bg} is the bottom-gate voltage and ε_0 is the vacuum permittivity. In Supplementary Fig. 4a, we fixed D = 0; therefore, $V_{bg} = C_{tg}/C_{bg} \times V_{tg}$ and the carrier density can be expressed as $n = 2C_{tg}V_{tg}/e$. Supplementary Fig. 4c shows the Hall density as a function of V_{tg}, and the linear fit will give $2C_{tg}$. Two gate voltages $V_{tg(full)}$ and $V_{bg(full)}$ corresponding to the full filling of the flat band in the $R_{xx}(V_{tg}, V_{bg})$ mapping can be obtained. Full carrier density is then expressed as $N_f = (C_{tg}V_{tg(full)} + CV_{bg(full)})/e$.

Single-particle continuum model description of the supermoiré band structure

To model mirror-asymmetric alternating trilayer graphene, we consider a commensurate approximation, taking $\theta_{1,2} = p\theta$ and $\theta_{2,3} = -q\theta$, where our system approximately corresponds to $(p, q) = (3, 4)$. Following ref. 38, we write down the local Hamiltonian for this system in the K valley as follows:

$$H^K_{TBG} = \begin{pmatrix} v_F\mathbf{k}\cdot\boldsymbol{\sigma} + \Delta U & w_{1\leftrightarrow 2}T(p\mathbf{r}) & 0 \\ w_{1\leftrightarrow 2}T^\dagger(p\mathbf{r}) & v_F\mathbf{k}\cdot\boldsymbol{\sigma} & w_{2\leftrightarrow 3}T^\dagger(q\mathbf{r}-\mathbf{d}) \\ 0 & w_{2\leftrightarrow 3}T(q\mathbf{r}-\mathbf{d}) & v_F\mathbf{k}\cdot\boldsymbol{\sigma} - \Delta U \end{pmatrix}, \quad (1)$$

where v_F is the graphene Dirac velocity, $w_{1\leftrightarrow 2}$ ($w_{2\leftrightarrow 3}$) is a dimensionless parameter that allows to tune the tunnellings between the first and second (second and third) layers, $\boldsymbol{\sigma}$ is the vector of Pauli matrices in sublattice space, $\mathbf{k}$ is the crystal momentum measured relative to the K-valley Dirac point, $\mathbf{r}$ is the real space position vector in the 2D graphene plane and ΔU is an interlayer potential difference used to model an external displacement field. The tunnelling term reads

$$\begin{aligned} T(\mathbf{r}) = {} & (w_{AA}\sigma_0 + w_{AB}\sigma_x)e^{i\mathbf{q}_1\cdot\mathbf{r}} \\ & + (w_{AA}\sigma_0 + w_{AB}\sigma_x e^{2\pi i/3\sigma_z})e^{i\mathbf{q}_2\cdot\mathbf{r}} + \\ & + (w_{AA}\sigma_0 + w_{AB}\sigma_x e^{4\pi i/3\sigma_z})e^{i\mathbf{q}_3\cdot\mathbf{r}}, \end{aligned} \quad (2)$$

where w_{AA} parameterizes the strength of intrasublattice tunnelling and w_{AB} is the strength of intersubattice tunnelling. Above $\mathbf{q}_j = \frac{4\pi\theta}{3a_0}(O_3)^j\,[0, -1]$, where a_0 is the monolayer graphene lattice constant and O_3 is the matrix of a counterclockwise 120° rotation. The vector $\mathbf{d}$ parameterizes[14] the displacement of the third layer with respect to the first layer.

To gain an intuitive understanding of the band structures, we fix the strength of tunnelling between the first and second layers to the TBG values $w_{1\leftrightarrow 2} = 1$, but treat $w_{2\leftrightarrow 3}$ as a tuning parameter. We use v_F = 542.1 meV nm, w_{AB} = 110 meV, $w_{AA} = 0.7w_{AB}$ and $\mathbf{d} = \mathbf{d}_{AB}$, where $\mathbf{d}_{AB} = \theta a_0(\frac{1}{2\sqrt{3}}, -\frac{1}{2})$ is the location of the AB-stacking point for TBG at twist angle θ. We use the twist angle θ = 0.45°, giving $\theta_{1,2}$ = 1.35° and $\theta_{2,3}$ = −1.8°, close to the values of our device. To model an applied displacement field, we also vary the interlayer potential difference ΔU. We show the resulting band structures in Extended Data Fig. 5 for four values of $w_{2\leftrightarrow 3}$ and four values of ΔU, showing the increasing hybridization of the third-layer Dirac cone for increasing $w_{2\leftrightarrow 3}$, as well as the shifting of the Dirac cone with ΔU. The purpose of this modelling is not to quantitatively reproduce the data, but to rather provide an intuitive explanation for how a robust Dirac cone could arise in a symmetry-broken TTG.

Data availability

Source data are provided with this paper. These data are also available via Zenodo at https://doi.org/10.5281/zenodo.17403996 (ref. 41). All other data that support the findings of this study are available from the corresponding author upon request.

References

41. Banerjee, M. Strong correlations and superconductivity in the supermoiré lattice. *Zenodo* https://doi.org/10.5281/zenodo.17403996 (2025).

Acknowledgements

We thank A. Stern, Y. Oreg, J. L. Lado and K. Ensslin for fruitful discussions. Z.Z. acknowledges funding from SNSF. K.K. was supported by Deutsche Forschungsgemeinschaft through CRC 183 (project C02). C.L. was supported by start-up funds from the Florida State University and the National High Magnetic Field Laboratory. The National High Magnetic Field Laboratory is supported by the National Science Foundation through NSF/DMR-2128556 and the State of Florida. M.B. acknowledges support from SNSF Eccellenza grant number PCEGP2_194528, and support from the QuantERA II Programme that has received funding from the European Union's Horizon 2020 research and innovation programme under grant agreement number 101017733. K.W. and T.T. acknowledge support from the JSPS KAKENHI (grant numbers 20H00354 and 23H02052) and World Premier International Research Center Initiative (WPI), MEXT, Japan.

Author contributions

M.B. supervised the project. Z.Z. fabricated the devices, performed the measurements and analysed the data, with help from C.S. C.S., K.K. and C.L. conducted the theory calculations. K.W. and T.T. provided the hBN crystals. Z.Z. wrote the paper with input from all authors.

Competing interests

The authors declare no competing interests.

Additional information

Extended data is available for this paper at https://doi.org/10.1038/s41567-025-03131-0.

Supplementary information The online version contains supplementary material available at https://doi.org/10.1038/s41567-025-03131-0.

Correspondence and requests for materials should be addressed to Mitali Banerjee.

Peer review information *Nature Physics* thanks the anonymous reviewers for their contribution to the peer review of this work.

 https://doi.org/10.1038/s41567-025-03131-0

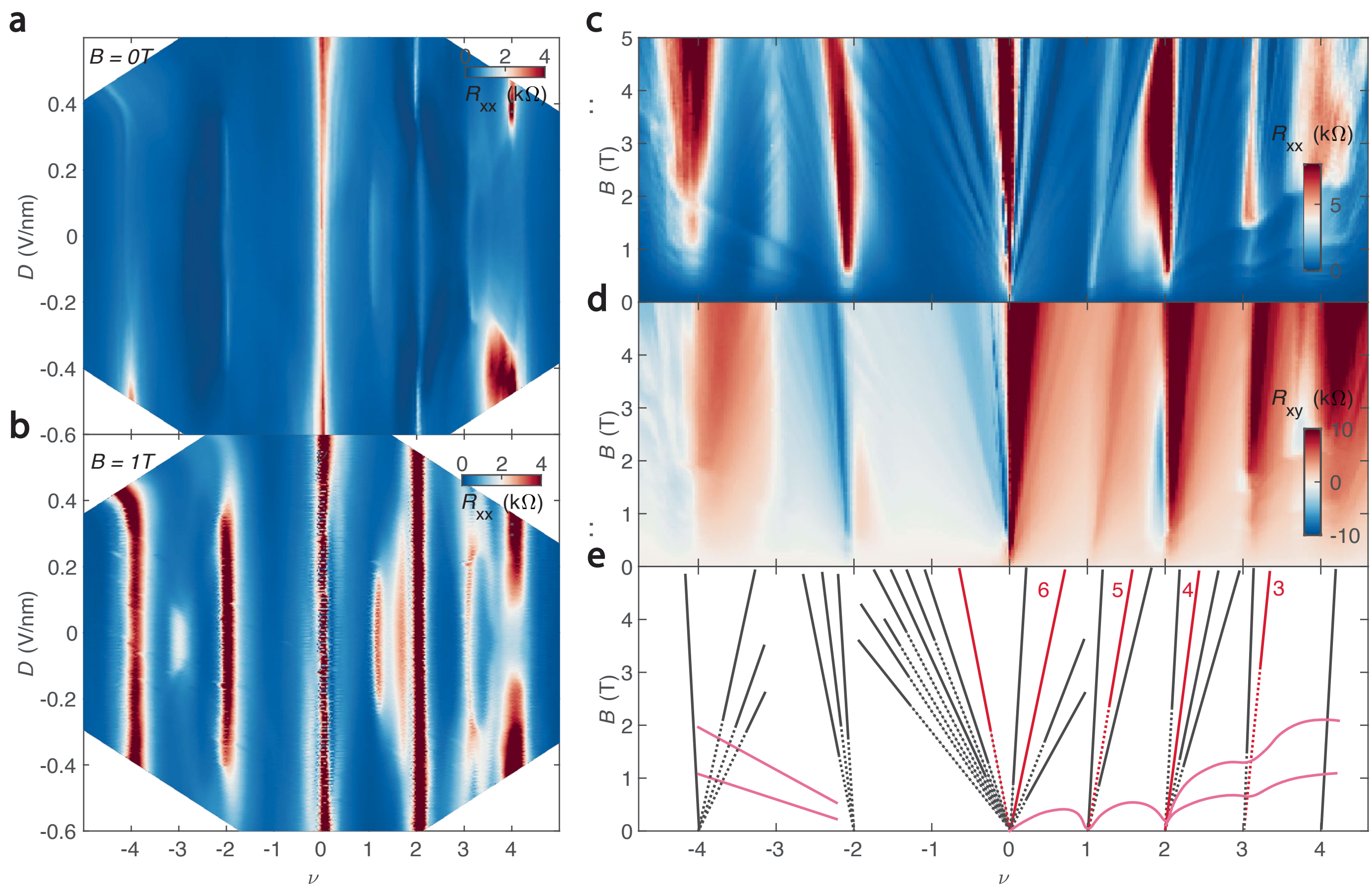

Extended Data Fig. 1 | Results of a twisted trilayer graphene device with mirror symmetry where $\theta_{12} = -\theta_{23} = 1.35^{\circ}$. a–b, R_{xx} as function of ν and D when $B = 0$ T (**a**) and $B = 1$ T (**b**) at T = 240 mK. Superconductivity appears on both the hole-doped side and electron-doped side. Correlated states appear at moiré filling $\nu = 1, \pm 2, 3$. The result is symmetric with respect to the displacement field, reflecting the device's mirror symmetry. **c-d**, Landau fan diagram of R_{xx} (**c**) and R_{xy} (**d**) at $D = 0$ V/nm. **e**, The states shown in (**c**) and (**d**). Landau levels originating from $\nu = \pm 4, 0$ and $\nu = 1, \pm 2, 3$ are visible, as indicated by the black and red lines, while those from the Dirac band are shown in pink. The red lines mark the most robust Landau levels stemming from each correlated state at ν and have a slope of $C = 2 + 4 - \nu$ in the fan diagram. Dirac Landau levels contribute $C_{Dirac} = 2$, and $C_{flat} = 2 + 4 - \nu$ originates from symmetry-broken Chern insulators in flat bands, similar to those observed in TBG.

https://doi.org/10.1038/s41567-025-03131-0

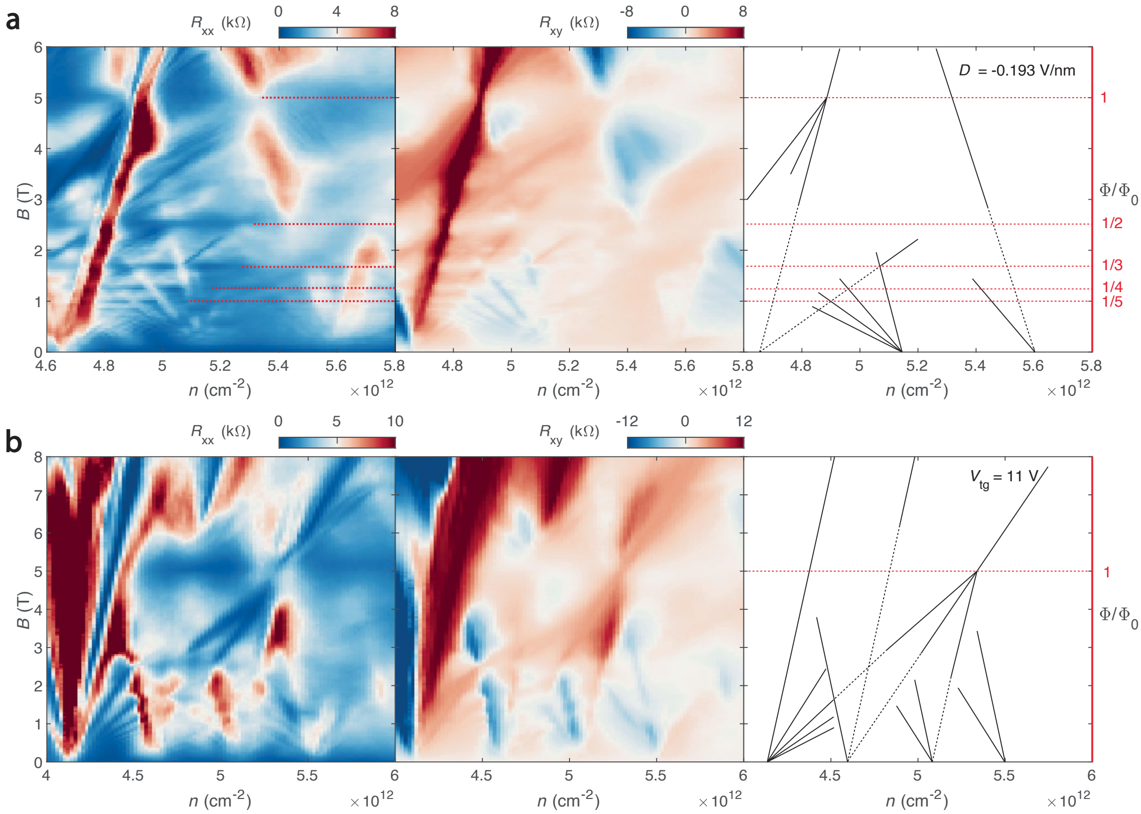

Extended Data Fig. 2 | Landau levels from the supermoiré lattice at different points in the *n* − *D* mapping. **a**, R_{xx} and R_{xy} as a function of B and n when $D = -0.193$ V/nm. The right figure extracted the states by black lines, and the red lines mark 1, 1/2, 1/3… quantum flux of the supermoiré lattice. Landau levels stemming from different supermoiré minibands are visible. **b**, the same measurement as **a** with fixing top gate voltage $V_{tg} = 11$ V and varying V_{bg} to change carrier density. Four sets of Landau levels can be seen and the distance between each is n_{sm}. (T = 11 mK).

 https://doi.org/10.1038/s41567-025-03131-0

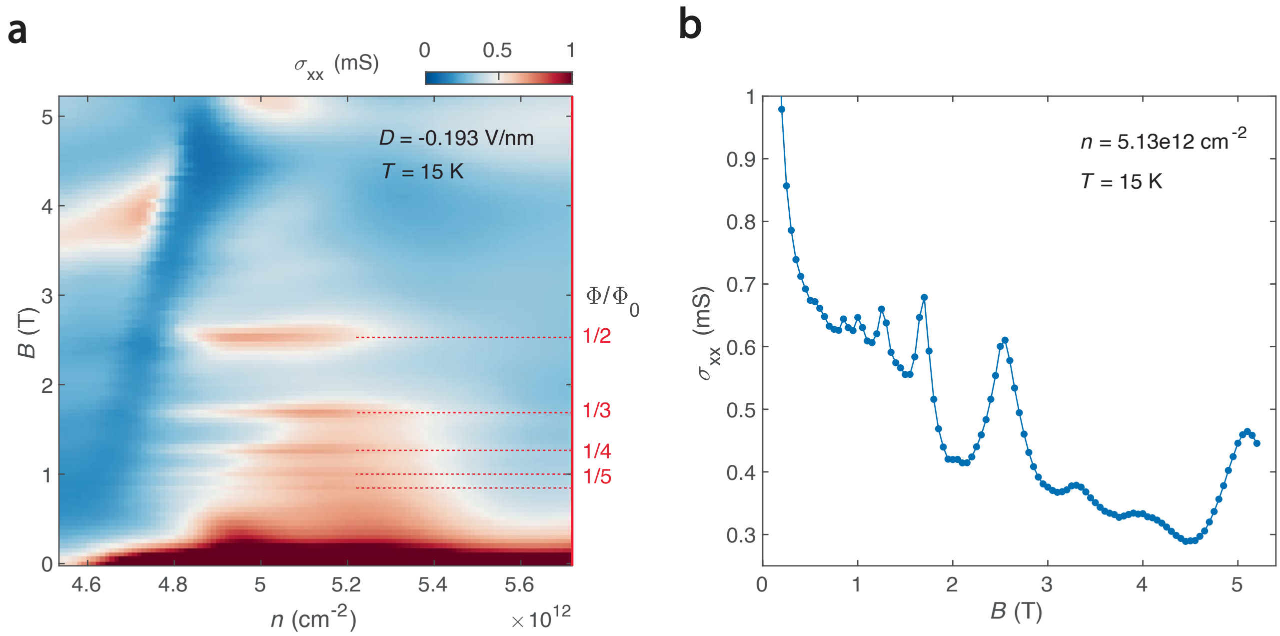

Extended Data Fig. 3 | Supermoiré Brown-Zak oscillation. a, Longitudinal conductance as a function of n and B at T = 15 K. The conductance shows peaks at the fractional quantum flux of the supermoiré lattice, suggesting the Brown-Zak oscillation. **b**, Line cut of conductance at a fixed carrier density from **a**.

https://doi.org/10.1038/s41567-025-03131-0

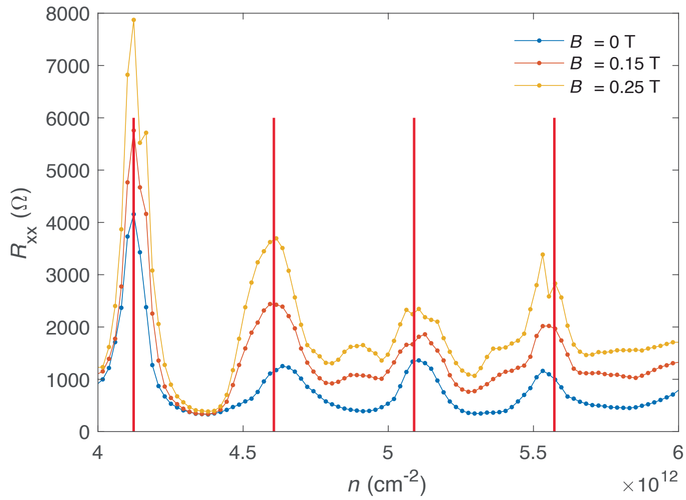

Extended Data Fig. 4 | Period oscillation of R_{xx} at high doping region. The longitudinal resistance R_{xx} is plotted as a function of carrier density for a fixed top gate voltage of V_{tg} = 11 V under different magnetic fields. Red lines serve as guides to the eye, indicating the expected positions of resistance peaks. The spacing between successive red lines corresponds to $n_{sm} = 0.468 \times 10^{12}$ cm^{-2}. The first resistance peak consistently aligns with the corresponding red guiding line. The second resistance peak shows a slight deviation from the red line; however, at B = 0.15 T and B = 0.25 T, it aligns well with the guiding lines. The third and fourth resistance peaks exhibit small deviations from the red lines.

https://doi.org/10.1038/s41567-025-03131-0

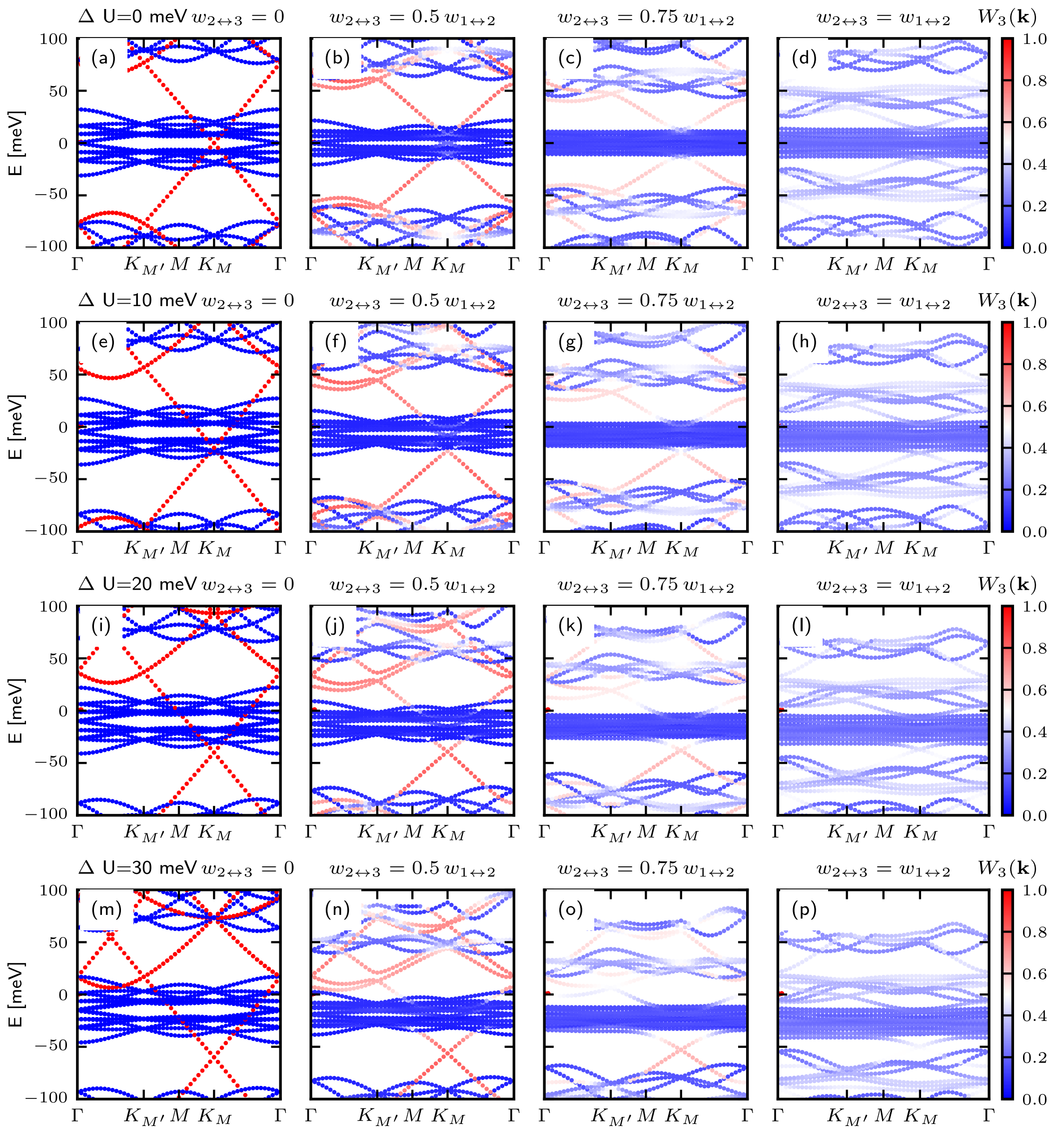

Extended Data Fig. 5 | Hybridization of the Dirac cone with the mini bands as a function of interlayer tunnelling. a–p, The single particle electronic structure of the TTG is tracked as a function of interlayer potential difference ΔU and interlayer tunnelling between layer 2 and layer 3. The band color indicates the extent of state polarization on the bottom layer (layer 3). In the weak tunnelling regime, the Dirac band exists and the relative fermi surface between mini bands and Dirac band can be adjusted by the displacement field. **a**-**d** show the band structure at $\Delta U = 0$ meV. **e**-**h** show the band structure at $\Delta U = 10$ meV. **i**-**l** show the band structure at $\Delta U = 20$ meV. **m**-**p** show the band structure at $\Delta U = 30$ meV.

https://doi.org/10.1038/s41567-025-03131-0

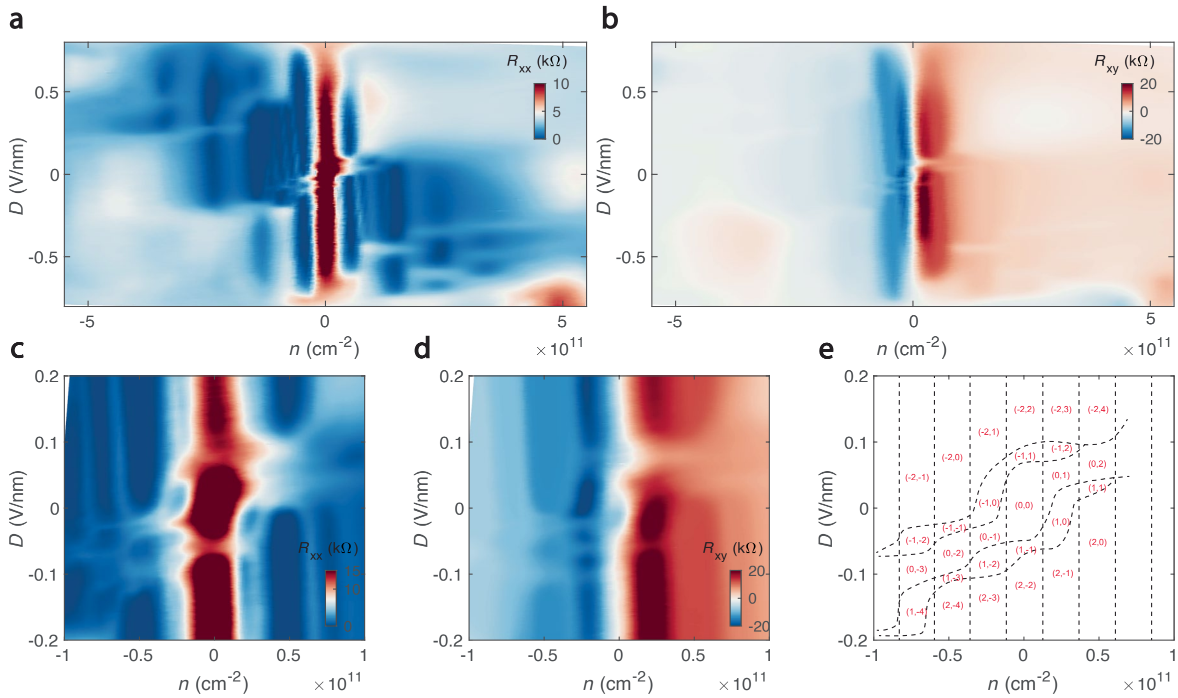

Extended Data Fig. 6 | Coexisting of Dirac band and flat band, with co-propagating and counter-propagating edge states near the CNP. a–**b**, $n-D$ mapping of R_{xx} and R_{xy} when $B=1$ T. Same as in Fig. 2e,f, vertical features are flat band Landau levels, and 'S' shape features are the transition lines of nearby Dirac Landau levels. However, compared with the results measured at $B=0.5$ T, the distance between different vertical features equals eB/h, which means the four-fold degeneracy of flat band Landau levels is lifted. **c**-**e**, Zoom-in of R_{xx} (**c**) and R_{xy} (**d**). The degeneracy of Dirac band Landau levels is also lifted. There are four Dirac Landau level transition lines near CNP, between which N_{Dirac} equals 1, 0, −1. At a fixed n, the number of total filled Landau levels $N_{total}=nh/eB$ and the filled flat band Landau levels $N_{flat}=N_{total}-N_{Dirac}$ can be extracted. **e**, Figure shows (N_{Dirac}, N_{flat}) in the $n-D$ mapping. ($T=240$ mK).

https://doi.org/10.1038/s41567-025-03131-0

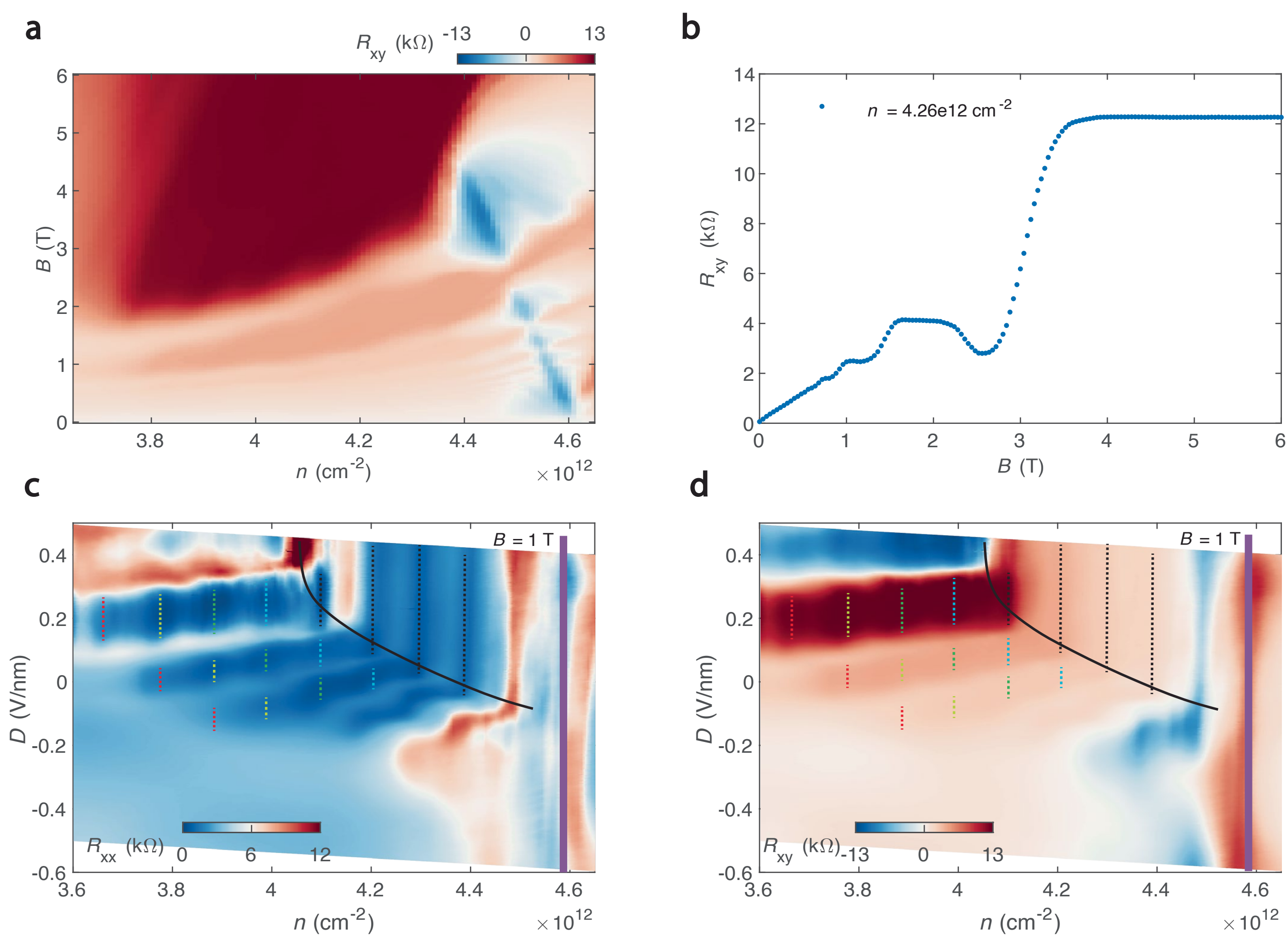

Extended Data Fig. 7 | Isospin symmetry breaking in the supermoiré mini band. a, the corresponding Landau fan diagram of R_{xy} of the R_{xx} shown in Fig. 3a. **b**, Line cut of R_{xy} at a carrier density of $n = 4.26 \times 10^{12}$ cm^{-2}. R_{xy} shows almost quantized resistance values of h/e^2, $h/2e^2$, $h/6e^2$, and $h/10e^2$, attributed to the Dirac Landau levels. When the Fermi level lies within the gap of the flat band, the transport is solely governed by the Dirac band, which transitions into Dirac Landau levels in the presence of a magnetic field. **c**-**d**, $n-D$ mapping of R_{xx} and R_{xy} at $B = 1$ T for electron densities near the full filling of the top moiré lattice. The black solid lines indicate the full filling of the top moiré lattice. It is evident that the position of this full filling shifts as a function of the displacement field. This shift arises from the relative band shift between the Dirac band and the flat band. When the displacement field becomes sufficiently large (in our case, $D > 0.3$ V/nm), the Dirac band hybridizes with the flat band. As a result, R_{xy} no longer exhibits characteristics associated with the Dirac band. The purple lines mark the strong states appearing at $n_{12} + n_{sm}$, which occur when the Fermi level lies within the gap of both the Dirac and flat bands. Additionally, the red dashed line highlights a gapped state induced by the supermoiré lattice. Between the red and black lines, three more states marked by yellow, green, and cyan lines are observed. These are attributed to isospin symmetry breaking within the supermoiré miniband.

https://doi.org/10.1038/s41567-025-03131-0

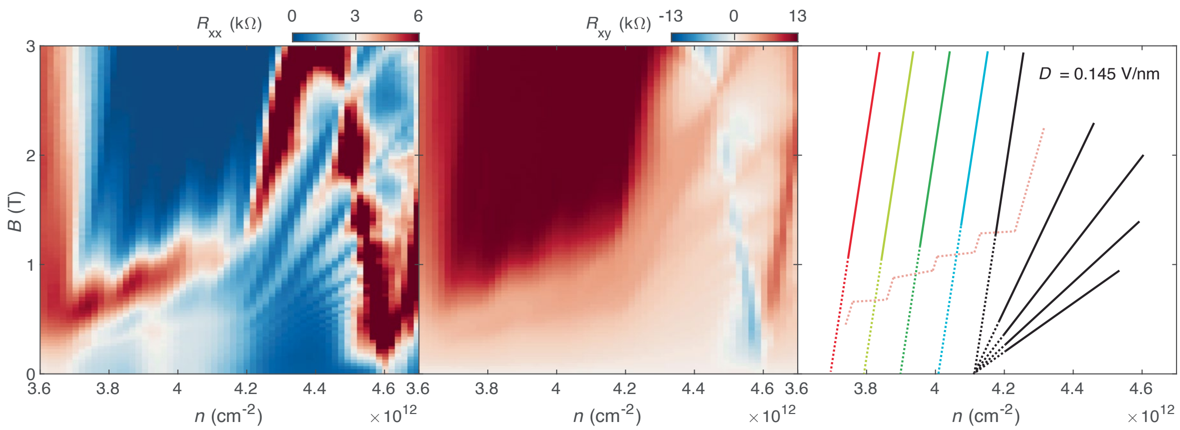

Extended Data Fig. 8 | Evidence of Isospin symmetry broken phases in mini band at D = 0.145 V/nm. Landau fan diagram of R_{xx} and R_{xy} at D = 0.145 V/nm. All the observed features in the Landau fan are illustrated. The black dashed lines represent Landau levels originating from the full filling of the top moiré lattice (n_{12}). The red dashed line marks the gapped state induced by the supermoiré lattice. The pink line indicates the transition between different Dirac Landau level regimes and above this line, two Dirac Landau levels are filled; below it, due to a change in degeneracy, six Dirac Landau levels are filled. Additionally, three states highlighted by yellow, green, and cyan lines are observed, with spacings $n_{sm}/4$. These are isospin symmetry broken states within the supermoiré mini band.

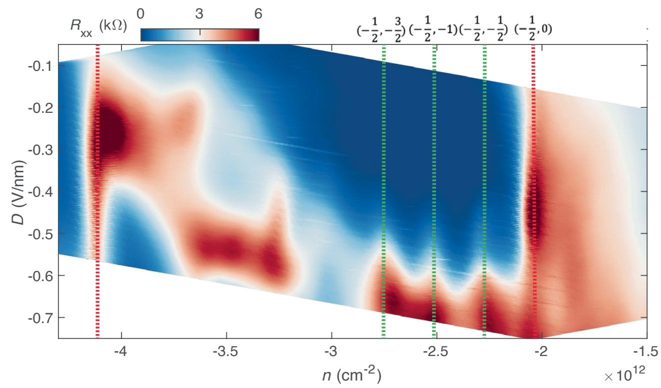

Extended Data Fig. 9 | Cascade of superconductor-insulator transitions on the hole-doped side. $n-D$ mapping of R_{xx} on the hole-doped side. The red dashed lines mark the half filling ($\frac{1}{2} * n_{12}$) and full filling (n_{12}) states of the top moiré lattice. The green dashed lines are the guiding lines for the other resistive states appearing in the superconducting regime. And the distance between is $\frac{1}{2} * n_{sm}$. Similar to Fig. 4a, the nature of these states depends on the relative strength between interaction effects and the supermoiré potential.

https://doi.org/10.1038/s41567-025-03131-0

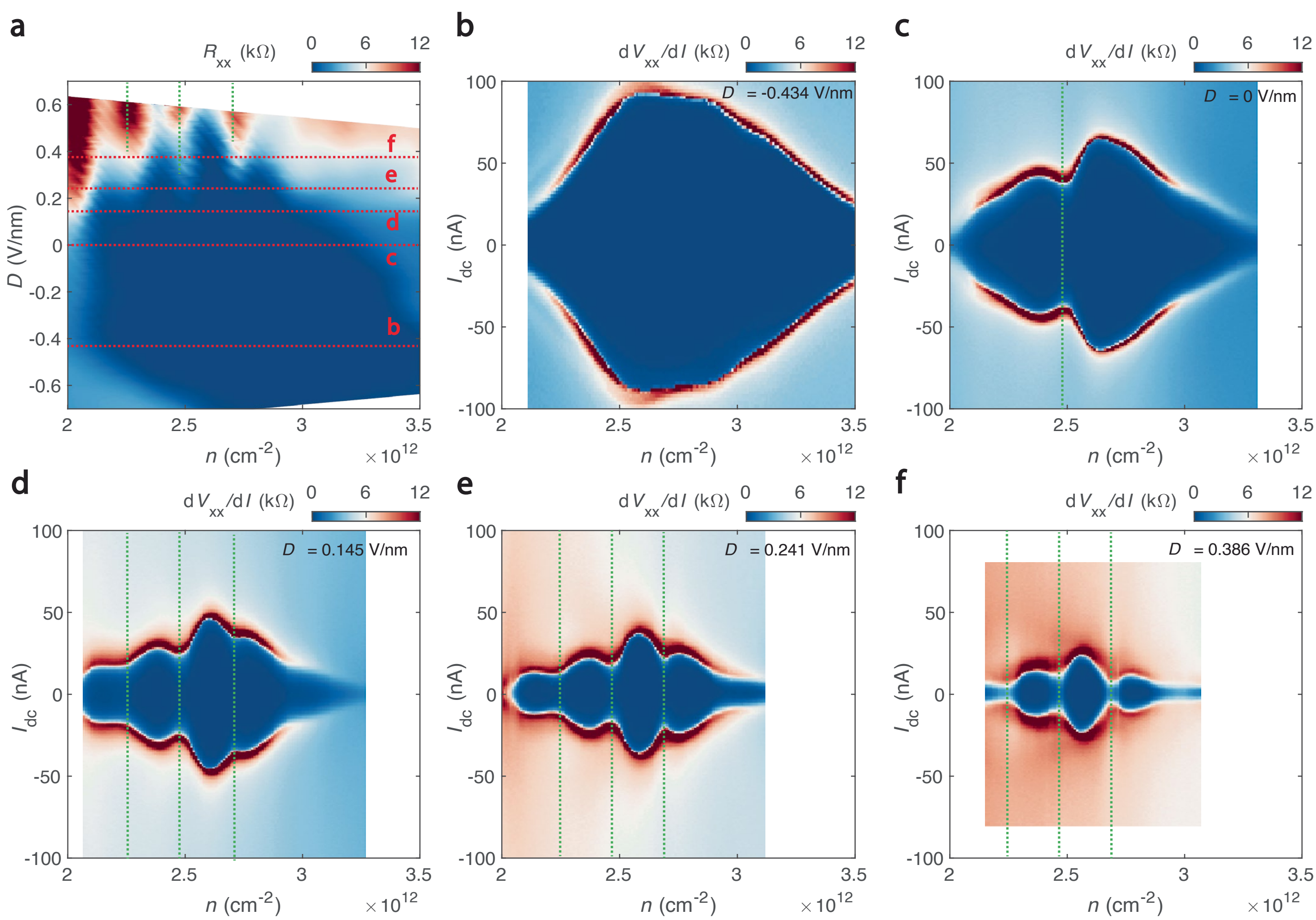

Extended Data Fig. 10 | Displacement field dependence of superconductivity. **a**, $n-D$ mapping of R_{xx} at T = 240 mK. **b**–**e**, dV_{xx}/dI versus I_{dc} and n at different displacement fields. At a very large negative displacement field (**b**), superconductivity shows a single superconducting dome with the maximum critical current around 100 nA. As the displacement field increases, superconductivity weakens, and the maximum critical current decreases. More interestingly, the superconductor is gradually diced into small superconducting domes. At D = 0 V/nm, the critical current shows a kink in the superconducting dome as marked by the green dashed line where the carrier density is $\frac{1}{2} * n_{12} + n_{sm}$. This shows that the supermoiré lattice starts mediating the superconductivity. At higher displacement fields, there are critical current kinks features appearing as marked by green dashed lines in **d**, **e**, and **f**. The carrier density at these green lines corresponds to the half filling of supermoiré minibands. This indicates the appearance of symmetry-broken phases in mini flat bands. (T = 240 mK).